## RetinaRegNet: A Zero-Shot Approach for Retinal Image Registration

Vishal Balaji Sivaraman<sup>a</sup>, Muhammad Imran<sup>b</sup>, Qingyue Wei<sup>c</sup>, Preethika Muralidharan<sup>d</sup>, Michelle R. Tamplin<sup>e</sup>, Isabella M. Grumbach<sup>e</sup>, Randy H. Kardon<sup>e</sup>, Jui-Kai Wang<sup>f</sup>, Yuyin Zhou<sup>g</sup> and Wei Shao<sup>a,b,d,h,\*</sup>

flowa City VA Center for the Prevention and Treatment of Visual Loss, Department of Ophthalmology and Visual Sciences, Department of Electrical and Computer Engineering, University of Iowa, Iowa City, Iowa, 52242, United States.

#### ARTICLE INFO

#### Keywords: Retinal image registration Zero-shot image registration Inverse consistency Outlier detector

#### ABSTRACT

We introduce RetinaRegNet, a zero-shot image registration model designed to register retinal images with minimal overlap, large deformations, and varying image quality. RetinaRegNet addresses these challenges and achieves robust and accurate registration through the following steps. First, we extract features from the moving and fixed images using latent diffusion models. We then sample feature points from the fixed image using a combination of the SIFT algorithm and random point sampling. For each sampled point, we identify its corresponding point in the moving image using a 2D correlation map, which computes the cosine similarity between the diffusion feature vectors of the point in the fixed image and all pixels in the moving image. Second, we eliminate most incorrectly detected point correspondences (outliers) by enforcing an inverse consistency constraint, ensuring that correspondences are consistent in both forward and backward directions. We further remove outliers with large distances between corresponding points using a global transformationbased outlier detector. Finally, we implement a two-stage registration framework to handle large deformations. The first stage estimates a homography transformation to achieve global alignment between the images, while the second stage uses a third-order polynomial transformation to estimate local deformations. We evaluated RetinaRegNet on three retinal image registration datasets: color fundus images, fluorescein angiography images, and laser speckle flowgraphy images. Our model consistently outperformed state-of-the-art methods across all datasets. The accurate registration achieved by RetinaRegNet enables the tracking of eye disease progression, enhances surgical planning, and facilitates the evaluation of treatment efficacy. Our code is publicly available at: https://github. com/mirthAI/RetinaRegNet.

#### 1. Introduction

Image registration is a fundamental technique in medical imaging, with diverse applications including image-guided radiation therapy (Foskey et al., 2005), disease progression monitoring (Gorbunova et al., 2008), motion tracking (Shao et al., 2021b), brain mapping (Toga and Thompson, 2001), and image fusion (Shao et al., 2021a). The goal of image registration is to align a moving (source) image with a fixed (target) image by estimating a geometric transformation that matches corresponding features or structures in the two images. In this study, we focus on retinal image registration, which enables the monitoring of eye disease progression and the assessment of treatment effectiveness (Saha et al., 2019). The main challenges in retinal image registration include estimating large deformations, registering images with minimal overlap, and ensuring robustness to variations in image quality (Can et al., 2002). Large deformations

🕍 weishao@ufl.edu (W. Shao)

ORCID(s): 0000-0003-4931-4839 (W. Shao)

involve the alignment of images with notable differences in position or scale, which often result in overfitting in transformation estimation or complicate point correspondence estimation. Small overlap between the fixed and moving images presents challenges since it can complicate the identification of corresponding features necessary for accurate alignment. Additionally, variations in image quality, caused by pathologies or differences in illumination, contrast, or noise levels, can further complicate the registration process, making it difficult to achieve a robust and accurate transformation. Overcoming these challenges requires the development of advanced algorithms that can handle complex transformations and remain robust to the inherent variability in retinal images.

To address the challenges in retinal image registration, we advocate for feature-based registration methods, starting with a feature point detector, followed by image feature extraction and matching, and transformation estimation. The most widely used feature point detector is the Scale-Invariant Feature Transform (SIFT) algorithm (Lowe, 2004), which

<sup>&</sup>lt;sup>a</sup>Department of Electrical and Computer Engineering, University of Florida, Gainesville, Florida, 32610, United States.

<sup>&</sup>lt;sup>b</sup>Department of Medicine, University of Florida, Gainesville, Florida, 32610, United States.

<sup>&</sup>lt;sup>c</sup>Department of Computational and Mathematical Engineering, Stanford University, Stanford, California, 94305, United States.

<sup>&</sup>lt;sup>d</sup>Department of Health Outcomes and Biomedical Informatics, University of Florida, Gainesville, Florida, 32610, United States.

<sup>&</sup>lt;sup>e</sup>Iowa City VA Center for the Prevention and Treatment of Visual Loss, Department of Internal Medicine, University of Iowa, Iowa City, Iowa, 52242, United States.

<sup>&</sup>lt;sup>g</sup>Department of Computer Science and Engineering, University of California, Santa Cruz, Santa Cruz, California, 95064, United States.

<sup>&</sup>lt;sup>h</sup>Intelligent Clinical Care Center, University of Florida, Gainesville, Florida, 32610, United States.

<sup>\*</sup>Corresponding author

can detect and describe rotation- and scaling-invariant local image features like corners and blobs. However, SIFT has limitations when applied to retinal image registration. First, most detected feature points tend to cluster in areas with rich textural features, leading to sparse or nonexistent point correspondences in homogeneous regions without distinctive features. Second, the image features generated by SIFT provide only a localized perspective, often leading to outliers in feature matching for image pairs with large deformations or minimal overlap. Two primary approaches have been developed to overcome the limitations of SIFT. One approach focuses on developing more efficient feature detectors, including general-purpose detectors (Alcantarilla et al., 2012; Bay et al., 2006) as well as those tailored for specific registration applications (Liu et al., 2022; Nasser et al., 2023; Wang et al., 2011). The other approach is detector-free, involving the extraction of two-dimensional (2D) feature maps from both fixed and moving images to compute a four-dimensional (4D) correlation map (Rocco et al., 2018). This map facilitates the identification of more feature point correspondences in regions with fewer distinct features.

In this paper, we introduce RetinaRegNet, a zero-shot model that achieves state-of-the-art performance on various retinal image registration tasks through several innovations. First, we sampled feature points from regions with rich features (e.g., edges, corners) and regions without distinct features to ensure that feature points are distributed throughout the images. This significantly improved registration accuracy in homogeneous regions. Second, our model reliably identified point correspondences using the concept of the inverse consistency constraint (Christensen and Johnson, 2001; Fua, 1992), which was originally used to ensure that if two images are registered to each other and then reversely registered, the estimated transformations are inverses of each other. In the context of estimating point correspondences between two images, inverse consistency is a necessary condition to ensure the correspondences are consistent in both the forward and backward directions. Third, our model excluded incorrect point correspondences where points have a long distance using a transformation-based outlier detector. The most widely used RANSAC (Random Sample Consensus) outlier-detection algorithm (Fischler and Bolles, 1981) relies on random sampling, which can lead to inconsistent results and increased computational time, especially when dealing with complex data with many outliers. Finally, our model utilized a two-stage registration framework. The first stage involved estimating a homography deformation to achieve a global alignment of the two images. This enabled step two, which was the estimation of a more accurate non-rigid local transformation. This two-stage design enhanced both the robustness and accuracy of our model.

We evaluated RetinaRegNet against leading retinal registration methods using three retinal image registration datasets. In the public FIRE dataset (Hernandez-Matas et al., 2017) of color fundus images, when compared to the best existing method, RetinaRegNet improved the AUC from

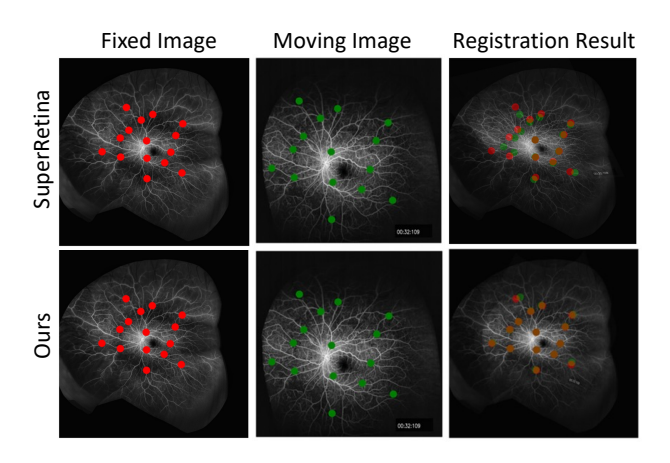


Figure 1: Visual comparison of the performance of RetinaReg-Net and SuperRetina (Liu et al., 2022) when registering an image pair with large displacement and scaling deformations. Red points represent landmarks on the fixed image, and green points represent the corresponding landmarks on the moving image. In the third column, the deformed images are overlaid with the fixed image, and landmarks on both the fixed and deformed images are shown in this overlay. The results demonstrate that our registration model significantly improves the alignment of the landmarks. The improved registration results are also evident in the much sharper overlaid image produced by our model.

0.779 to 0.901 and reduced the mean landmark error from 6.01 to 2.97. In the public FLoRI21 dataset (Ding et al., 2021) of fluorescein angiography images, when compared to the best existing method, RetinaRegNet improved the AUC of the second-best method from 0.640 to 0.868 and reduced the mean landmark error from 36.49 to 13.83. In the private LSFG dataset of laser-speckle flowgraphy images, when compared to the best existing methods, RetinaRegNet improved the AUC of the second-best method from 0.853 to 0.861 and reduced the mean landmark error from 4.23 to 4.00. This state-of-the-art performance across various retinal image datasets affirmed RetinaRegNet's significant potential in revolutionizing retinal image registration.

In summary, this paper makes the following key contributions:

- We introduced RetinaRegNet, a zero-shot retinal image registration model capable of registering retinal images with large deformations and minimal overlap.
- We demonstrated RetinaRegNet's state-of-the-art performance across three retinal image registration datasets.
- We evaluated the significance of each component in RetinaRegNet through comprehensive ablation studies.

## 2. Related Work

#### 2.1. Retinal Image Registration

Existing retinal image registration methods can be divided into two categories: intensity-based methods and

feature-based methods, or a combination of the two (Wang et al., 2015). Intensity-based image registration methods typically utilize an intensity similarity function (e.g., mutual information, cross-correlation, sum of squared differences) to align the intensity differences between two images (Legg et al., 2013; Molodij et al., 2015; Zhu, 2007). While intensity-based registration methods may achieve promising results, they are susceptible to overfitting when dealing with images exhibiting large deformations, minimal overlap, and variations in illumination and texture (Wang et al., 2015). Additionally, the choice of the similarity function is task-specific due to variations in imaging modality. In contrast, feature-based registration methods rely on image features such as vasculature bifurcations, the fovea, and the optic disc for transformation estimation. Feature-based methods are generally more robust compared to intensitybased methods. Due to these advantages, numerous featurebased retinal image registration techniques have been developed, using both conventional (Hernandez-Matas et al., 2020; Motta et al., 2019; Wang et al., 2019) and learningbased approaches (Chen et al., 2015; Lee et al., 2019; Liu and Li, 2023; Santarossa et al., 2022; Sun et al., 2021; Wang et al., 2020; Zou et al., 2020). Learning-based techniques outperform conventional methods by achieving higher accuracy, robustness, and efficiency, but they often require extensive preprocessing (Chen et al., 2015; Wang et al., 2020; Zou et al., 2020) or training on large datasets (Lee et al., 2019; Liu and Li, 2023; Santarossa et al., 2022; Sun et al., 2021).

#### 2.2. Semantic Correspondences

The goal of semantic correspondence is to identify and match similar semantic features across different images. This process often involves finding correspondences between objects (e.g., points, lines, or regions) based on their semantic meaning rather than visual similarities. Semantic correspondence typically relies on advanced deep learning methods, including convolutional neural networks and vision transformers, to extract and link these semantically similar elements across varied visual representations (Han et al., 2017; Liu et al., 2020; Zhao et al., 2021). There are two major differences between semantic correspondence and image registration. First, semantic correspondence identifies point correspondences by matching semantic features instead of visual features. Consequently, the images in semantic correspondence can depict two different objects, for example, birds of different species, which are not of interest in image registration. Second, while image registration aims to identify one-to-one point correspondences between two images, semantic correspondence seeks to establish sparse point correspondences (not necessarily one-to-one) between parts of images that share the same underlying features.

## 2.3. Diffusion Models

Denoising diffusion models (Ho et al., 2020; Kingma et al., 2021; Rombach et al., 2022; Song et al., 2020) have emerged as a leading class of generative models renowned for their capacity to generate high-quality images. These

models function by iteratively refining an initial Gaussian noise image through a series of reverse diffusion steps, which gradually diminishes noise and enhances image quality. Diffusion models have demonstrated promising performance across various applications, including image denoising (Gong et al., 2023), image super-resolution (Li et al., 2022), image inpainting (Lugmayr et al., 2022), image segmentation (Amit et al., 2021), and image-to-image generation (Jiang et al., 2024). Training and sampling diffusion models in the original image space can be computationally expensive. A more efficient approach is to conduct the forward and reverse diffusion processes in a smaller latent image space. A prime example of this is stable diffusion (Rombach et al., 2022), which has subsequently been repurposed for numerous generation tasks such as text-to-3D conversion (Poole et al., 2022) and image editing (Mokady et al., 2023). Stable diffusion features have recently found applications in representation learning (Yang and Wang, 2023) and semantic correspondences (Hedlin et al., 2023; Tang et al., 2024).

#### 3. Method

Figure 2 provides an overview of our RetinaRegNet image registration model. Inspired by the application of diffusion features (DIFT) in semantic correspondence (Tang et al., 2024), our model began by extracting image features using a pre-trained stable diffusion model (Rombach et al., 2022). Subsequently, we sampled key feature points in the fixed image using a combination of the SIFT algorithm and random point sampling. This approach allowed for the extraction of feature points in areas with both rich and poor textures. For each sampled feature point in the fixed image, we computed a 2D correlation map to identify its corresponding point in the moving image. To remove outliers in the estimated point correspondences, we used an inverse consistency constraint combined with a transformation-based outlier detector. These strategies were crucial for significantly improving the accuracy and robustness of our registration model.

#### 3.1. Diffusion Feature Extraction

We briefly describe the extraction of diffusion image features proposed in (Tang et al., 2024). The forward diffusion process is a Markov chain that starts with a noise-free image and gradually adds noise to it over T steps, transforming the image into pure Gaussian noise. The model then learns to reverse this process, starting with a pure noise image and gradually removing noise from the image to generate new data samples. In latent diffusion models, the diffusion process primarily occurs in the latent space. At each time step t, noise is added to the latent image  $z_{t-1}$  to generate  $z_t$  with the following equation:

$$q(z_t|z_{t-1}) := \mathcal{N}(z_t; \sqrt{1 - \beta_t} z_{t-1}, \beta_t \mathbf{I})$$
(1)

where  $0 < \beta_0 < \dots < \beta_T << 1$  is a noise scheduler.

The reverse process involves training a model  $\epsilon_{\theta}(z_t, t)$ , typically implemented as a U-Net, to predict the Gaussian

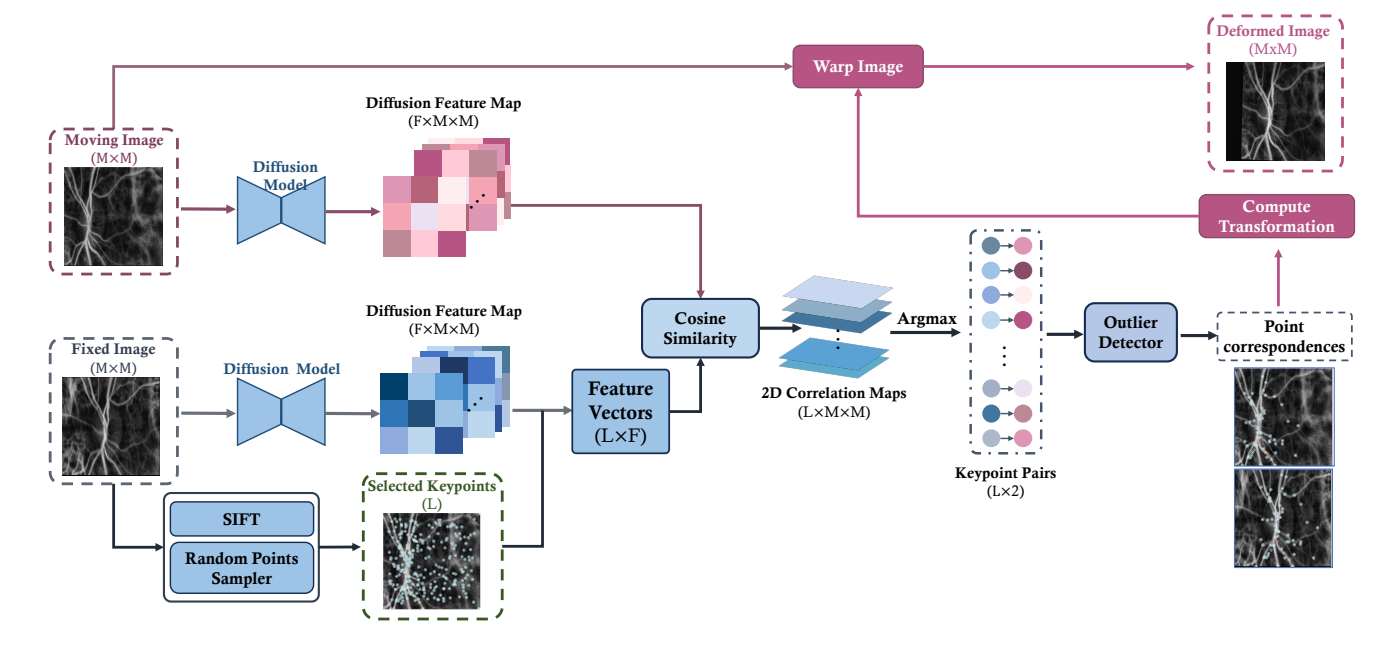


Figure 2: Overview of the proposed RetinaRegNet model for retinal image registration.

noise  $\epsilon$  added at each step of the forward process. The reverse process is represented as:

$$z_{t-1} = \frac{1}{\sqrt{\alpha_t}} \left( z_t - \frac{1 - \alpha_t}{\sqrt{1 - \bar{\alpha}t}} \epsilon_{\theta}(z_t, t) \right) + \sigma_t \mathbf{z}$$
 (2)

where 
$$\alpha_t = 1 - \beta_t$$
,  $\bar{\alpha}_t = \prod_{s=1}^t \alpha_s$ ,  $\sigma_t^2 = \frac{1 - \bar{\alpha}_{t-1}}{1 - \bar{\alpha}_t} \beta_t$ , and  $\mathbf{z} \sim \mathcal{N}(\mathbf{0}, \mathbf{I})$ 

To generate diffusion features of a high-quality image  $x_0$ , we initially encoded the image into the latent representation  $z_0$  using the encoder of a pre-trained autoencoder. Then, we introduced random noise to  $z_0$  by selecting a time step t and calculating the noisy image using:  $z_t = \sqrt{\bar{a}_t}z_0 + (1-\bar{a}_t)\epsilon_t$ , where  $\epsilon_t$  represents a random noise sample from  $\mathcal{N}(\mathbf{0},\mathbf{I})$ . Subsequently,  $z_t$  was fed into the U-Net denoiser, and we extracted features from intermediate layers to serve as diffusion images features.

#### 3.2. Feature Point Extraction

The goal of this step was to identify candidate feature points in the fixed image for which we identified corresponding points in the moving image. The SIFT algorithm (Lowe, 2004) is a widely used feature extraction algorithm in computer vision for detecting and describing local features in images that are invariant to scaling and rotation. We first employed the SIFT algorithm to detect K feature points in the fixed image, ensuring that the distance between any two feature points was greater than a threshold value,  $T_{sift}$ . For certain applications, such as retinal images, feature points detected by the SIFT algorithm were concentrated in the sparsely distributed vessel trees, which may have caused the estimated transformation to be less accurate in regions without densely distributed vessels. To address this issue,

in addition to the feature points detected by the SIFT algorithm, we randomly sampled an additional K feature points throughout the fixed image to improve the estimation of point correspondences, especially in homogeneous image regions. These points were randomly sampled such that they remained within the image boundary.

#### 3.3. Estimation of Point Correspondences

Given a high-resolution fixed image  $I_f$  of size  $H_f \times W_f$  and a moving image  $I_m$  of size  $H_m \times W_m$ , we first resampled both images to the size of  $M \times M$ . Diffusion image features were extracted using an intermediate layer of the denoising U-Net in a pre-trained stable diffusion model (Rombach et al., 2022). We upsampled the feature maps to the size of  $M \times M$ . The resulting diffusion features were denoted as  $D_f$  and  $D_m$ , with dimensions  $F \times M \times M$ , where F represents the size of each feature vector.

We sampled a list of L=2K feature points  $p_1,\cdots,p_L$  in the fixed image to find the point in the moving image corresponding to each  $p_i$ . We computed the cosine similarity score between  $D_f(p_i)$  and the feature vector of every pixel in the moving image. The pixel with the highest similarity score was considered to correspond to  $p_i$ . For computational efficiency, we combined the diffusion feature vectors at all feature points into a matrix  $[D_f(p_1),\cdots,D_f(p_L)]$  of size  $L\times F$ . We then computed a 2D correlation map for each feature point, resulting in a correlation map  $C=[C_1,\cdots,C_L]$  which consisted of L 2D correlation maps:

$$C = \mathbf{norm}([D_f(p_1), \cdots, D_f(p_L)]^T) * \mathbf{norm}(D_m)$$
(3)

where the **norm** operation was applied to each feature vector to convert it into a vector of unit norm, and \* is matrix multiplication.

The correlation map C is of dimension  $L \times M \times M$ , such that each feature point corresponds to a 2D correlation map. We then applied the Argmax operation to each of the L correlation maps to obtain the corresponding points in the moving image, i.e.,

$$[p'_1, \cdots, p'_L] = [\operatorname{Argmax}(C_1), \cdots, \operatorname{Argmax}(C_L)]$$
 (4)

## 3.4. Outlier Detector

Point correspondences estimated by the 2D correlation maps can contain errors (outliers) due to variations in image quality. To address this, we designed a two-stage outlier detector that effectively eliminates these outliers from the estimated correspondences, enhancing the robustness of the transformation estimation between image pairs.

Inverse Consistency Based Outlier Detector. Inverse consistency (Christensen and Johnson, 2001; Fua, 1992) was originally used in pairwise image registration to ensure that the forward and backward transformations estimated between two images are inverses of each other. In this paper, we applied this concept to remove outliers in point correspondences between two images. For each feature point  $p_i$  in the fixed image, we first determined its corresponding point  $p'_i$  in the moving image using a 2D correlation map. Then, we reversed the roles of the fixed and moving images and used the same method to identify the point  $p_i''$  in the fixed image that corresponds to  $p'_i$ . A necessary criterion for the accuracy of estimating point correspondences using 2D correlation maps was the proximity of  $p_i$  to  $p_i''$ . We considered the point correspondence  $(p_i, p'_i)$  accurate if it met the following condition; otherwise, we considered this correspondence an outlier and removed it from the estimation of the geometric transformation:

$$||p_i - p_i''||_2 \le T_{IC},\tag{5}$$

where  $T_{IC}$  represents the inverse consistency threshold.

Transformation Based Outlier Detector. The estimation of a geometric transformation based on point correspondences is sensitive to outliers. The RANSAC algorithm (Fischler and Bolles, 1981) is one of the most widely used outlier detectors. It iteratively selects a random subset of the original data, fits a model, and then evaluates how many of the remaining data points conform to this model within a predefined tolerance. While conceptually straightforward and easy to implement, RANSAC can be computationally intensive for large datasets or complex models. Its performance heavily relies on the chosen threshold for distinguishing inliers from outliers and the number of iterations.

We observed that the transformation estimation was most sensitive to outliers with large distances between the true corresponding point and the estimated corresponding point. Inspired by this observation, we proposed a simple yet effective transformation-based outlier detector. Given a set of estimated point correspondences  $(p_i, p_i')$  between two images, our method first estimates a global transformation (e.g., affine)  $\phi$  using all the point correspondences. The

global transformation is then applied to each point  $p_i$ , resulting in transformed points  $\phi(p_i)$ . The accuracy of each point correspondence is evaluated by computing the Euclidean distance between  $\phi(p_i)$  and  $p_i'$ . Point correspondences with a distance greater than a threshold  $T_{trans}$  were removed. This process can be summarized by the following:

$$(p_i, p_i')$$
 is an outlier if  $||\phi(p_i) - p_i'||_2 \ge T_{trans}$  (6)

## 3.5. Multi-Stage Image Registration Framework

We designed our registration model as a multi-stage framework to handle large variations in the underlying transformation between images through a coarse-to-fine strategy. In the first stage, we estimated a global transformation  $\psi_{global}$  between the two images, where estimating such a global transformation is less sensitive to outliers than a more complex local transformation. In the second stage, we estimated a local deformation  $\psi_{local}$  between the globally aligned image pairs. The composition of these two transformations gave the final transformation between the two images, i.e.,  $\psi = \psi_{local} \circ \psi_{global}$ . We have implemented four distinct types of transformation models: affine transformation (6 degrees of freedom), homography transformation (8 degrees of freedom), quadratic transformation (12 degrees of freedom), and third-order polynomial transformation (20 degrees of freedom). For all experiments in this study, we chose the homography transformation model in the first stage for global alignment, followed by the third-order polynomial transformation model in the second stage to refine local feature alignment.

## 4. Experiments

#### 4.1. Datasets

We used three retinal image registration datasets for model evaluation: color fundus, fluorescein angiography, and laser speckle flowgraphy. These different modalities capture retinal images for various applications, including diagnosing retinal conditions, assessing treatment outcomes, and monitoring retinal blood flow dynamics.

**FIRE Dataset** The first dataset we used is the public FIRE (Fundus Image Registration Dataset) dataset (Hernandez-Matas et al., 2017) that contains 129 color fundus images that form 134 image pairs. Acquired using a Nidek AFC-210 fundus camera at the Papageorgiou Hospital from 39 patients, the dataset offered a resolution of 2912×2912 pixels with a field of view (FOV) of 45°. The FIRE dataset provided ground truth correspondences for 10 landmark points for each image pair. These landmark points were manually selected by an annotator, primarily focusing on vessels and crossings, to ensure broad coverage of the overlapping image areas. Image pairs in the FIRE dataset were divided into three categories. Class S consists of 71 image pairs characterized by high spatial overlap (greater than 75%) and no significant visual anatomical differences, making them easy to register. Class P consists of 49 pairs with a small overlap (less than 75%), making these pairs hard to register. Finally, Class A includes 14 image pairs with considerably large

overlap. This exhibits visual anatomical differences which make them moderately hard to register.

**FLoRI21 Dataset** The second dataset we used was the public FLoRI21 (Fluorescein-angiography Longitudinal Retinal Image 2021) dataset (Ding et al., 2021) which consists of 15 pairs of ultra-wide-field fluorescein angiography (FA) images taken 24 weeks apart for each subject. These images were captured using Optos California (Nikon Co. Ltd, Japan) and 200Tx cameras. Each image pair had one montage FA image (4000  $\times$  4000) used as the fixed image, and several raw FA images (3900  $\times$  3072) used as the moving images. Ten pairs of landmark points were chosen at retinal vessel bifurcations, ensuring coverage of the entire overlapping image area.

LSFG Dataset The third dataset we used was an Institutional Review Board-approved laser speckle flowgraphy (LSFG) dataset that contains 15 pairs of longitudinal LSFG images from patients with uveal melanoma. These patients were treated at the University of Iowa with <sup>125</sup>I-plaque brachytherapy. LSFG (Softcare Co., Japan) is non-invasive and can measure mean blur rate, which is linearly proportional to blood flow velocity at the retina and optic nerve head in a video clip of 118 time frames. We averaged each pixel value along the aligned time-sequence frames of the LSFG video to create a 2D blood flow map (751 × 420). Each LSFG image pair has 6-10 ground truth landmark correspondences which were selected by a human annotator.

#### 4.2. Methods for Comparison

We compared our RetinaRegNet model with six recent image registration methods. Among these, the GFEMR algorithm (Wang et al., 2019) tackles the registration problem through a probabilistic approach which integrates manifold regularization to preserve the retina's intrinsic geometry. Another method, ASpanFormer (Chen et al., 2022), uses an adaptive span transformer to find point correspondences. This employs CNN encoders and iterative global-local attention blocks which utilize auxiliary flow maps to adapt local attention span based on matching uncertainty. Another method we considered was SuperGlue (Sarlin et al., 2020), a neural network that matches two sets of local features by jointly finding correspondences and rejecting non-matchable points. Additionally, SuperRetina (Liu et al., 2022), employs a trainable keypoint detector and descriptor. It is trained using semi-supervised learning with a combination of labeled and unlabeled images; however, it requires manual or automatic labeling and is subject to keypoint detection errors and mismatches. Moreover, we also considered the LoFTR algorithm (Sun et al., 2021), which uses a transformer network to create feature descriptors from both images, establishing dense correspondences at a coarse level before refining them. Lastly, GeoFormer (Liu and Li, 2023), another general-purpose method based on LoFTR, leverages RANSAC geometry to identify attentive regions and uses the transformer's cross-attention mechanism for feature matching during transformation estimation.

## 4.3. Evaluation Metrics

**Mean Landmark Error** Given a pair of fixed and moving images, we have a set of N manually annotated landmark pairs. Each landmark point in one image is denoted as  $(x_i, y_i)$ , and its corresponding ground truth landmark point in the other image is denoted as  $(x_i', y_i')$ . Let  $\psi$  represent a geometric transformation that we have estimated to align the fixed image with the moving image. The mean landmark error (MLE) for this pair of images is defined as the mean of the Euclidean distance between each transformed point  $(x_i'', y_i'') := \psi(x_i, y_i)$  and its corresponding ground truth point  $(x_i', y_i')$ . Mathematically, the MLE can be expressed as:

$$MLE = \frac{1}{N} \sum_{i=1}^{N} \sqrt{(x_i'' - x_i')^2 + (y_i'' - y_i')^2}$$
 (7)

Area Under the Curve The normalized area under the curve (AUC) evaluates an image registration method by assessing its performance at various MLE thresholds ([0,  $T_{AUC}$ ]). For each threshold value, a registration is considered accurate if its MLE is below the threshold. A registration accuracy, indicating the proportion of accurately registered images, is computed for the entire image set at each threshold. The normalized AUC metric integrates these success rates across all MLE thresholds which provides a comprehensive assessment of registration accuracy. Mathematically, the normalized AUC can be expressed as

$$AUC = \frac{1}{T_{AUC}} \int_0^{T_{AUC}} RA(T)dT \tag{8}$$

where RA(T) denote the registration accuracy at the threshold value T.

**Registration Success Rate** We categorize the image registration of an image pair as unsuccessful under either of two conditions. Firstly, the registration is considered failed if there are insufficient point correspondences to estimate the required geometric transformation. For example, a minimum of 3 pairs of points is necessary to estimate an affine transformation, and at least 6 pairs are needed for a quadratic transformation. Secondly, the registration is considered unsuccessful if the mean landmark error exceeds a predetermined threshold,  $T_{SR}$ , which is determined by the specific characteristics of the registration dataset. By applying these criteria, we can calculate the success rate of each registration method across different datasets. In this paper, we chose  $T_{SR} = \frac{1}{2}T_{AUC}$ .

#### 4.4. Implementation Details

The proposed model was implemented using PyTorch and Diffusers on a computing node equipped with two CPU cores, 25 GB of RAM, and a NVIDIA A100 GPU. For image registration, images from the FIRE, FLoRI21, and LSFG datasets were resampled to resolutions of  $920 \times 920$ ,  $1024 \times 1024$ , and  $740 \times 740$  pixels, respectively. After registration, the coordinates of corresponding points were upsampled to

their original image sizes for transformation estimation and landmark error evaluation. We extracted K = 1000 feature keypoints from the moving image using the SIFT algorithm, ensuring that the distance between any two keypoints was greater than 10 pixels. Additionally, we randomly selected another set of K = 1000 feature points from the moving image.Diffusion image features were extracted using the third layer of the denoising U-Net at time step t = 1 for each dataset. The inverse consistency threshold was set at  $T_{IC} = 3$  pixels for all datasets. For the computation of the AUC, threshold values  $(T_{AUC})$  were set at 25, 100, and 25 for the FIRE, FLoRI21, and LSFG datasets, respectively. For the transformation-based outlier detector, we selected the affine transformation model for both registration stages and set threshold values  $(T_{trans})$  to 25 and 15 for the FIRE dataset, 40 and 30 for FLoRI21, and 25 and 25 for the LSFG datasets, respectively. A higher threshold was selected for the FLoRI21 dataset to accommodate its predominantly nonaffine deformation in image pairs.

#### 5. Results

#### **5.1.** Quantitative Evaluation

Results on the FIRE Dataset. Table 1 demonstrates that our model significantly outperformed all other methods in the challenging *P* class of hard-to-register cases, delivering the highest AUC of 0.856, compared to the 0.697 AUC of the second-best method, GFEMR. These results underscore our model's superior ability to handle large displacement deformations and small overlaps between images. Furthermore, in the other two classes, our model achieved state-of-the-art performance, significantly improving the overall AUC across the FIRE dataset from 0.779 (achieved by SuperRetina) to 0.901, and reducing the mean landmark error from 6.01 to 2.97. Additionally, our model proved to be the most robust, achieving a registration success rate of 99.25%, significantly surpassing the 91.04% success rate of GFEMR.

Results on the FLoRI21 Dataset Challenges in registering image pairs in the FLoRI21 dataset are primarily from the large displacement and scaling deformations between the montage and raw FA images. The results presented in Table 2 show that our model significantly outperformed the second-best performing model, GeoFormer, in several key metrics. Specifically, our model achieved an AUC of 0.868 compared to GeoFormer's 0.640, a mean landmark error of 13.83 versus 36.49, and a 100% registration success rate, substantially higher than GeoFormer's 93.33%. It was notable that AspanFormer, GFEMR, LoFTR, SuperGlue, and SuperRetina all struggled to achieve accurate registration in at least 20% of the cases. In particular, GFEMR, which is customized for registering color fundus images, was not well-suited for addressing the large scaling and displacement deformations in another retinal dataset. This resulted in a high mean landmark error of 71.58 and a low success rate of 6.67%.

**Table 1** Registration results on the FIRE Dataset. MLE: mean landmark error. Success rate threshold:  $T_{SR} = 12.5$ .

| Method      | Easy  | Moderate | Hard  | FIRE  | MLE   | Success Rate |
|-------------|-------|----------|-------|-------|-------|--------------|
| GFEMR       | 0.849 | 0.534    | 0.697 | 0.761 | 6.11  | 91.04%       |
| ASpanFormer | 0.878 | 0.728    | 0.057 | 0.562 | 18.05 | 64.92%       |
| SuperGlue   | 0.810 | 0.602    | 0.417 | 0.645 | 9.59  | 70.89%       |
| LoFTR       | 0.941 | 0.746    | 0.338 | 0.703 | 8.29  | 74.06%       |
| SuperRetina | 0.946 | 0.771    | 0.539 | 0.779 | 6.01  | 83.58%       |
| GeoFormer   | 0.922 | 0.757    | 0.564 | 0.774 | 6.14  | 88.80%       |
| Ours        | 0.951 | 0.805    | 0.856 | 0.901 | 2.97  | 99.25%       |

**Table 2** Registration results on the FLoRI21 Dataset. MLE: mean landmark error. Success rate threshold:  $T_{SR}=50$ .

| Method      | AUC   | MLE   | Success Rate |
|-------------|-------|-------|--------------|
| GFEMR       | 0.299 | 71.58 | 6.67%        |
| ASpanFormer | 0.548 | 45.59 | 60.00%       |
| SuperGlue   | 0.604 | 40.09 | 80.00%       |
| LoFTR       | 0.486 | 51.99 | 60.00%       |
| SuperRetina | 0.590 | 41.47 | 80.00%       |
| GeoFormer   | 0.640 | 36.49 | 93.33%       |
| Ours        | 0.868 | 13.83 | 100%         |
|             |       |       |              |

Table 3 Registration results on the LSFG Dataset. MLE: mean land-mark error. Success rate threshold:  $T_{SR}=12.5$ .

| Method      | AUC   | MLE   | Success Rate |
|-------------|-------|-------|--------------|
| GFEMR       | 0.587 | 15.29 | 73.33%       |
| ASpanFormer | 0.813 | 5.07  | 93.33%       |
| SuperGlue   | 0.752 | 6.66  | 93.33%       |
| LoFTR       | 0.853 | 4.23  | 100%         |
| SuperRetina | 0.843 | 4.32  | 100%         |
| GeoFormer   | 0.845 | 4.40  | 100%         |
| Ours        | 0.861 | 4.00  | 100%         |

Results on the LSFG Dataset. Image pairs in the LSFG dataset represent longitudinal measurements of blood flow in the eyes. The primary challenges in registering these LSFG image pairs arise from two factors: (1) positional shifts across images, attributable to the different times at which they were acquired, and (2) intensity variations across images, due to changes in blood flow over time. The results, as detailed in Table 3, demonstrate that our method outperformed all other methods in several key metrics. Specifically, our model achieved an AUC of 0.861, compared to the second-best method, LoFTR's 0.853, and a mean landmark error of 4.00, slightly better than LoFTR's 4.23.

Computational Complexity For each retinal registration dataset, we computed the average per-case running time of each image registration method. Results in Table ?? suggest that, although RetinaRegNet achieved state-of-theart performance on all three retinal registration datasets, it is the slowest method, taking up to 20 seconds to register each image pair. This extended running time is primarily due to the high computational cost associated with extracting diffusion features and computing 2D correlation maps for each feature point.

**Table 4** Per-case computational complexity (seconds).

| Method      | FIRE  | FLoRI21 | LSFG   |  |
|-------------|-------|---------|--------|--|
| GFEMR       | 3.032 | 5.313   | 0.9211 |  |
| ASpanFormer | 1.00  | 1.00    | 1.00   |  |
| SuperGlue   | 1.00  | 4.00    | 5.00   |  |
| LoFTR       | 0.363 | 0.508   | 0.324  |  |
| SuperRetina | 1.172 | 2.157   | 1.148  |  |
| GeoFormer   | 0.36  | 0.53    | 0.18   |  |
| Ours        | 13.00 | 19.00   | 18.00  |  |

## 5.2. Qualitative Evaluation

Figure 3 shows the registration results of one representative case from each of the three retinal image registration datasets. The corresponding landmarks in the fixed, moving, and deformed images demonstrate the high accuracy of our registration model across all three cases. The first row demonstrates that our model has successfully estimated the large displacement deformation between an image pair from the hard-to-register (P) category in the FIRE dataset. The second row shows how our model has accurately aligned an image pair with complex global and local deformations from the FLoRI21 dataset. The last row demonstrates the superior performance of our model on a pair of images in our LSFG dataset with large shifting. The consistently high performance of our model across all three datasets demonstrates its accuracy, robustness, as well as its potential to be utilized in other retinal image registration tasks.

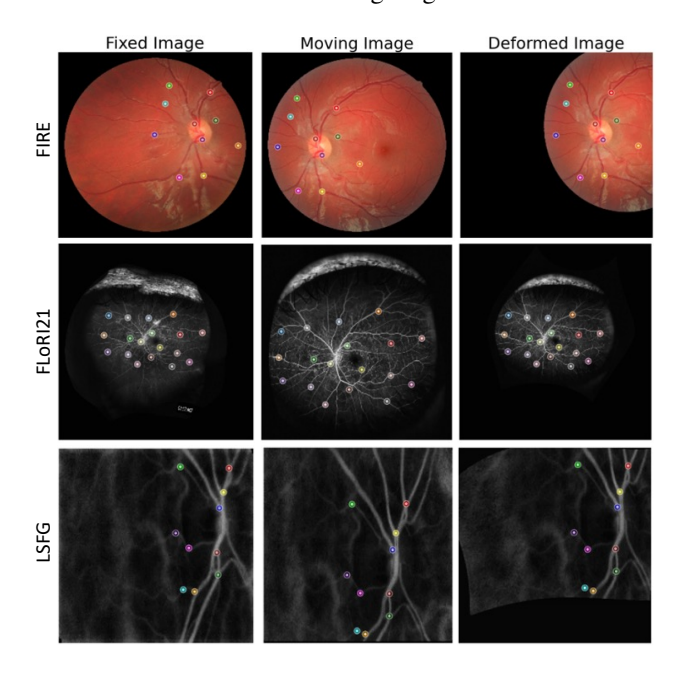


Figure 3: Registration results of the model are shown for the FIRE (first row), FLoRI21 (second row), and LSFG (third row) datasets. For each landmark, we assigned a unique color, consistent across fixed, moving, and deformed images, enabling clear observation of the alignment of each landmark pair.

**Table 5**AUC values of RetinaRegNet using different image feature extractors.

| Features           | FIRE  | FLoRI21 | LSFG  |
|--------------------|-------|---------|-------|
| CNN Features       | 0.894 | 0.860   | 0.791 |
| DINO-ViT Features  | 0.410 | 0.537   | 0.199 |
| Diffusion Features | 0.901 | 0.868   | 0.861 |

## 6. Ablation Study

## 6.1. Impact of Image Feature Extractor

We conducted an in-depth evaluation of the effectiveness of using different feature types in RetinaRegNet, including CNN features (Simonyan and Zisserman, 2014). vision transformer features (Caron et al., 2021), and diffusion features (Tang et al., 2024). Specifically, we utilized a pretrained VGG19 model for extracting CNN features, a pretrained 8-patch vision transformer network (ViT-S/8) for extracting DINO-ViT features, and a pretrained latent stable diffusion model (SDv2-1) for extracting diffusion features. We applied RetinaRegNet to re-register all pairs of images by replacing the diffusion features with the CNN features and DINO-ViT features. Registration results in Table ?? suggested that diffusion features achieved the best performance across all three datasets. RetinaRegNet achieved similar registration results on the FIRE and FLoRI21 datasets when using CNN features and diffusion features. However, the AUC of RetinaRegNet decreased from 0.861 to 0.791 on the LSFG dataset when using CNN features instead of diffusion features. Notably, the DINO-ViT features did not exhibit the same level of accuracy compared to the CNN features and diffusion features. Therefore, we chose to use diffusion features (DIFT) in the proposed RetinaRegNet registration framework.

#### 6.2. Impact of Diffusion Feature Size

Image features from various layers of the decoder in the stable diffusion model exhibit differing sizes, each smaller than the input image by a downsampling factor. We assessed how variations in diffusion feature size affect RetinaReg-Net's performance. Ideally, image features should capture high-level features without being either too shallow or too deep. Shallowness corresponds to a small downsampling factor with limited learned representations and deepness, corresponds to a large downsampling factor unsuitable for dense predictions due to excessively small image features.

Results in Table 6 indicated that the diffusion features corresponding to a downsampling factor of 32 exhibited the best registration performance across all three retinal datasets; these features provide a balance between detailed representation and abstraction. Diffusion features corresponding to a downsampling factor of 16 also achieved promising registration results, ranking second best. Notably, the features extracted from the first block and the last block both resulted in poor performance. These blocks represent extremely low and high-level diffusion features, respectively.

**Table 6**AUC values of RetinaRegNet using diffusion features extracted by different downsampling factors.

| Feature Selection | Downsampling Factor | FIRE  | FLoRI21 | LSFG  |
|-------------------|---------------------|-------|---------|-------|
| Block-1 Features  | 8                   | 0.086 | 0.000   | 0.000 |
| Block-2 Features  | 16                  | 0.742 | 0.796   | 0.834 |
| Block-3 Features  | 32                  | 0.901 | 0.868   | 0.861 |
| Block-4 Features  | 64                  | 0.554 | 0.301   | 0.051 |

Table 7
Impact of each model component on AUC values.

| Method                                   | FIRE  | FLoRI21 | LSFG  |
|--|-------|---------|-------|
| RetinaRegNet (proposed)                  | 0.901 | 0.868   | 0.861 |
| RetinaRegNet w/o inverse consistency     | 0.884 | 0.847   | 0.850 |
| RetinaRegNet w/o random point sampling   | 0.890 | 0.866   | 0.842 |
| RetinaRegNet w/o affine outlier detector | 0.805 | 0.835   | 0.416 |
| RetinaRegNet w/o multi-stage design      | 0.782 | 0.649   | 0.853 |

## 6.3. Impact of Key Model Components

We investigated the impact of each of the four key components in RetinaRegNet, including the inverse consistency constraint, the random feature point sampling strategy, the transformation-based outlier detector, and the multistage registration framework. We reran RetinaRegNet on all image pairs using one of the following: (1) removing the inverse consistency constraint; (2) omitting the random sampling strategy; (3) replacing the affine transformation-based outlier detector with the RANSAC outlier detector; and (4) replacing the multi-stage framework with a single-stage design.

Results in Table 7 indicate that all four components significantly contribute to the high performance of the RetinaRegNet model, although their impact varies across different retinal datasets. For instance, in both the FIRE dataset and the FLoRI21 dataset, the multi-stage image registration design notably improved performance by a significant margin, likely due to the complexity of deformations between image pairs in those two datasets. Conversely, in the LSFG dataset, substituting our affine transformation-based outlier detector with the RANSAC detector resulted in a significantly decreased AUC from 0.861 to 0.416, possibly due to the simpler nature of deformations in these images.

#### 7. Discussion

## 7.1. Clinical Implications

The retina, a light-sensitive layer at the back of the eye, plays a vital role in our vision (Kawamura and Tachibanaki, 2012). However, retinal diseases like diabetic retinopathy, glaucoma, and age-related macular degeneration (Chan et al., 2017; Duh et al., 2017; Imran et al., 2022; Lim et al., 2012) can lead to vision impairment. Early detection and treatment are crucial, emphasizing the need for monitoring retinal blood vessels. Retinal image registration, a technique used to align retinal images, facilitates accurate diagnosis and disease monitoring. By precisely tracking changes over time and assessing treatment response, clinicians can effectively manage retinal pathologies. Our RetinaRegNet,

achieving state-of-the-art registration accuracy, holds immense potential to revolutionize clinical practice by empowering clinicians with enhanced diagnostic tools and treatment monitoring capabilities, ultimately leading to improved patient outcomes.

#### 7.2. Limitations and Future Directions

Our study has several limitations. First, RetinaRegNet is computationally expensive, requiring between 10 to 20 seconds per image pair due to the computation of a 2D correlation map for each selected feature point in the moving images. In this paper, we opted for 2000 feature points (1000 for SIFT; 1000 for random point sampling), however users have the flexibility to choose a lower number of points, particularly when the underlying transformation between the two images is an affine or homography transformation. We will assess the trade-off between computational efficiency and registration accuracy in our future work. Second, our focus was solely on mono-modal image registration, which overlooked the generalization of our method to multimodal retinal image registration challenges. We plan to evaluate the effectiveness of RetinaRegNet in multi-modal registration by initially training and employing an imageto-image translation network to unify different modalities into a single modality, followed by applying RetinaRegNet. Third, theoretically, RetinaRegNet can serve as a general image registration approach that can be extended to various other registration tasks. In the future, we aim to evaluate RetinaRegNet's performance in other medical image registration contexts (e.g., registering 2D histopathology and MRI images) and nature image registration contexts (e.g., aligning images captured by unmanned aerial vehicles from different angles or times).

## 8. Conclusion

We introduced RetinaRegNet, a zero-shot image registration model designed to address the challenges of large deformations, minimal overlap, and varying image quality in retinal images. Through a novel combination of feature extraction using diffusion models, inverse consistency, outlier detection, and a two-stage registration framework, RetinaRegNet consistently outperformed state-of-theart methods across three retinal image registration datasets. Our comprehensive evaluation demonstrated its robust performance in registering images across different modalities, highlighting its potential for clinical applications such as disease monitoring and treatment evaluation. Despite some computational limitations, RetinaRegNet represents a significant advancement in retinal image registration.

#### **CRediT** authorship contribution statement

**Vishal Balaji Sivaraman:** Methodology, Software, Formal analysis, Investigation, Data curation, Writing - original draft, Visualization. **Muhammad Imran:** Methodology, Software, Writing - review & editing, Visualization.

Qingyue Wei: Methodology, Writing - review & editing, Visualization. Preethika Muralidharan: Data curation, Writing - review & editing. Michelle R. Tamplin: Data curation, Writing - review & editing. Isabella M. Grumbach: Data curation, Writing - review & editing. Randy H. Kardon: Data curation, Supervision, Writing - review & editing. Jui-Kai Wang: Data curation, Supervision, Writing - review & editing. Yuyin Zhou: Methodology, Supervision, Writing review & editing. Wei Shao: Conceptualization, Methodology, Resources, Data curation, Writing - original draft, Supervision, Project administration, Funding acquisition.

#### Conflict of interest statement

The authors have no conflict of interest to declare.

# Declaration of generative AI and AI-assisted technologies in the writing process

During the preparation of this work the authors used the ChatGPT-3.5 and ChatGPT-4.0 tools in order to improve the readability and language of our paper. After using this tool/service, the authors reviewed and edited the content as needed and take full responsibility for the content of the publication.

## Acknowledgments

This work was supported by the Department of Medicine and the Intelligent Clinical Care Center at the University of Florida College of Medicine. We would like to express our gratitude to Alexander Cosman for editing the language of this paper.

#### References

- Alcantarilla, P. F., Bartoli, A., and Davison, A. J. (2012). Kaze features. In Computer Vision–ECCV 2012: 12th European Conference on Computer Vision, Florence, Italy, October 7-13, 2012, Proceedings, Part VI 12, pages 214–227. Springer.
- Amit, T., Shaharbany, T., Nachmani, E., and Wolf, L. (2021). Segdiff: Image segmentation with diffusion probabilistic models. arXiv preprint arXiv:2112.00390.
- Bay, H., Tuytelaars, T., and Van Gool, L. (2006). Surf: Speeded up robust features. In Computer Vision–ECCV 2006: 9th European Conference on Computer Vision, Graz, Austria, May 7-13, 2006. Proceedings, Part 19, pages 404–417. Springer.
- Can, A., Stewart, C., Roysam, B., and Tanenbaum, H. (2002). A feature-based, robust, hierarchical algorithm for registering pairs of images of the curved human retina. *IEEE Transactions on Pattern Analysis and Machine Intelligence*, 24(3):347–364.
- Caron, M. et al. (2021). Emerging properties in self-supervised vision transformers. In *Proceedings of the IEEE/CVF international conference* on computer vision, pages 9650–9660.
- Chan, K. K., Tang, F., Tham, C. C., Young, A. L., and Cheung, C. Y. (2017).
  Retinal vasculature in glaucoma: a review. BMJ open ophthalmology, 1(1):e000032.
- Chen, H. et al. (2022). Aspanformer: Detector-free image matching with adaptive span transformer.
- Chen, L., Huang, X., and Tian, J. (2015). Retinal image registration using topological vascular tree segmentation and bifurcation structures. *Biomedical Signal Processing and Control*, 16:22–31.

- Christensen, G. E. and Johnson, H. J. (2001). Consistent image registration. IEEE transactions on medical imaging, 20(7):568–582.
- Ding, L. et al. (2021). Flori21: Fluorescein angiography longitudinal retinal image registration dataset. *IEEE Dataport*.
- Duh, E. J., Sun, J. K., and Stitt, A. W. (2017). Diabetic retinopathy: current understanding, mechanisms, and treatment strategies. JCI insight, 2(14).
- Fischler, M. A. and Bolles, R. C. (1981). Random sample consensus: a paradigm for model fitting with applications to image analysis and automated cartography. *Communications of the ACM*, 24(6):381–395.
- Foskey, M., Davis, B., Goyal, L., Chang, S., Chaney, E., Strehl, N., Tomei, S., Rosenman, J., and Joshi, S. (2005). Large deformation three-dimensional image registration in image-guided radiation therapy. *Physics in Medicine & Biology*, 50(24):5869.
- Fua, P. (1992). Fua, p.: A parallel stereo algorithm that produces dense depth. maps and preserves image features. machine vision and applications 6, 35-49. *Mach. Vis. Appl.*, 6:35-49.
- Gong, K., Johnson, K., El Fakhri, G., Li, Q., and Pan, T. (2023). Pet image denoising based on denoising diffusion probabilistic model. *European Journal of Nuclear Medicine and Molecular Imaging*, pages 1–11.
- Gorbunova, V., Lo, P., Ashraf, H., Dirksen, A., Nielsen, M., and de Bruijne, M. (2008). Weight preserving image registration for monitoring disease progression in lung ct. In Medical Image Computing and Computer-Assisted Intervention–MICCAI 2008: 11th International Conference, New York, NY, USA, September 6-10, 2008, Proceedings, Part II 11, pages 863–870. Springer.
- Han, K. et al. (2017). Scnet: Learning semantic correspondence. In Proceedings of the IEEE international conference on computer vision, pages 1831–1840.
- Hedlin, E. et al. (2023). Unsupervised semantic correspondence using stable diffusion. *arXiv preprint arXiv:2305.15581*.
- Hernandez-Matas, C., Zabulis, X., and Argyros, A. A. (2020). Rempe: Registration of retinal images through eye modelling and pose estimation. *IEEE journal of biomedical and health informatics*, 24(12):3362–3373.
- Hernandez-Matas, C., Zabulis, X., Triantafyllou, A., Anyfanti, P., Douma, S., and Argyros, A. A. (2017). Fire: fundus image registration dataset. Modeling and Artificial Intelligence in Ophthalmology, 1(4):16–28.
- Ho, J., Jain, A., and Abbeel, P. (2020). Denoising diffusion probabilistic models. Advances in neural information processing systems, 33:6840– 6851.
- Imran, M., Ullah, A., Arif, M., Noor, R., et al. (2022). A unified technique for entropy enhancement based diabetic retinopathy detection using hybrid neural network. *Computers in Biology and Medicine*, 145:105424.
- Jiang, H., Imran, M., Ma, L., Zhang, T., Zhou, Y., Liang, M., Gong, K., and Shao, W. (2024). Fast-ddpm: Fast denoising diffusion probabilistic models for medical image-to-image generation. arXiv e-prints, pages arXiv-2405.
- Kawamura, S. and Tachibanaki, S. (2012). Explaining the functional differences of rods versus cones. Wiley Interdisciplinary Reviews: Membrane Transport and Signaling, 1(5):675–683.
- Kingma, D., Salimans, T., Poole, B., and Ho, J. (2021). Variational diffusion models. Advances in neural information processing systems, 34:21696– 21707.
- Lee, J. A., Liu, P., Cheng, J., and Fu, H. (2019). A deep step pattern representation for multimodal retinal image registration. In *Proceedings* of the IEEE/CVF International Conference on Computer Vision, pages 5077–5086.
- Legg, P. A., Rosin, P. L., Marshall, D., and Morgan, J. E. (2013). Improving accuracy and efficiency of mutual information for multi-modal retinal image registration using adaptive probability density estimation. *Computerized Medical Imaging and Graphics*, 37(7-8):597–606.
- Li, H. et al. (2022). Srdiff: Single image super-resolution with diffusion probabilistic models. *Neurocomputing*, 479:47–59.
- Lim, L. S., Mitchell, P., Seddon, J. M., Holz, F. G., and Wong, T. Y. (2012).
  Age-related macular degeneration. *The Lancet*, 379(9827):1728–1738.
- Liu, J. and Li, X. (2023). Geometrized transformer for self-supervised homography estimation. In *Proceedings of the IEEE/CVF International* Conference on Computer Vision, pages 9556–9565.

- Liu, J., Li, X., Wei, Q., Xu, J., and Ding, D. (2022). Semi-supervised keypoint detector and descriptor for retinal image matching. In *European Conference on Computer Vision*, pages 593–609. Springer.
- Liu, Y., Zhu, L., Yamada, M., and Yang, Y. (2020). Semantic correspondence as an optimal transport problem. In *Proceedings of the IEEE/CVF Conference on Computer Vision and Pattern Recognition*, pages 4463–4472.
- Lowe, D. G. (2004). Distinctive image features from scale-invariant keypoints. *International journal of computer vision*, 60:91–110.
- Lugmayr, A., Danelljan, M., Romero, A., Yu, F., Timofte, R., and Van Gool, L. (2022). Repaint: Inpainting using denoising diffusion probabilistic models. In *Proceedings of the IEEE/CVF Conference on Computer Vision and Pattern Recognition*, pages 11461–11471.
- Mokady, R., Hertz, A., Aberman, K., Pritch, Y., and Cohen-Or, D. (2023).
  Null-text inversion for editing real images using guided diffusion models. In *Proceedings of the IEEE/CVF Conference on Computer Vision and Pattern Recognition*, pages 6038–6047.
- Molodij, G., Ribak, E. N., Glanc, M., and Chenegros, G. (2015). Enhancing retinal images by nonlinear registration. *Optics Communications*, 342:157–166.
- Motta, D., Casaca, W., and Paiva, A. (2019). Vessel optimal transport for automated alignment of retinal fundus images. *IEEE Transactions on Image Processing*, 28(12):6154–6168.
- Nasser, S. A., Gupte, N., and Sethi, A. (2023). Reverse knowledge distillation: Training a large model using a small one for retinal image matching on limited data. arXiv preprint arXiv:2307.10698.
- Poole, B., Jain, A., Barron, J. T., and Mildenhall, B. (2022). Dreamfusion: Text-to-3d using 2d diffusion. *arXiv preprint arXiv:2209.14988*.
- Rocco, I., Cimpoi, M., Arandjelović, R., Torii, A., Pajdla, T., and Sivic, J. (2018). Neighbourhood consensus networks. Advances in neural information processing systems, 31.
- Rombach, R., Blattmann, A., Lorenz, D., Esser, P., and Ommer, B. (2022). High-resolution image synthesis with latent diffusion models. In Proceedings of the IEEE/CVF conference on computer vision and pattern recognition, pages 10684–10695.
- Saha, S. K., Xiao, D., Bhuiyan, A., Wong, T. Y., and Kanagasingam, Y. (2019). Color fundus image registration techniques and applications for automated analysis of diabetic retinopathy progression: A review. Biomedical Signal Processing and Control, 47:288–302.
- Santarossa, M. et al. (2022). Medregnet: Unsupervised multimodal retinalimage registration with gans and ranking loss. In *Medical Imaging 2022: Image Processing*, volume 12032, pages 321–333. SPIE.
- Sarlin, P.-E., DeTone, D., Malisiewicz, T., and Rabinovich, A. (2020). Superglue: Learning feature matching with graph neural networks. In 2020 IEEE/CVF Conference on Computer Vision and Pattern Recognition (CVPR), pages 4937–4946.
- Shao, W., Banh, L., Kunder, C. A., Fan, R. E., Soerensen, S. J., Wang, J. B., Teslovich, N. C., Madhuripan, N., Jawahar, A., Ghanouni, P., et al. (2021a). Prosregnet: A deep learning framework for registration of mri and histopathology images of the prostate. *Medical image analysis*, 68:101919
- Shao, W., Pan, Y., Durumeric, O. C., Reinhardt, J. M., Bayouth, J. E., Rusu, M., and Christensen, G. E. (2021b). Geodesic density regression for correcting 4dct pulmonary respiratory motion artifacts. *Medical image analysis*, 72:102140.
- Simonyan, K. and Zisserman, A. (2014). Very deep convolutional networks for large-scale image recognition. arXiv preprint arXiv:1409.1556.
- Song, Y., Sohl-Dickstein, J., Kingma, D. P., Kumar, A., Ermon, S., and Poole, B. (2020). Score-based generative modeling through stochastic differential equations. arXiv preprint arXiv:2011.13456.
- Sun, J., Shen, Z., Wang, Y., Bao, H., and Zhou, X. (2021). Loftr: Detectorfree local feature matching with transformers. In *Proceedings of the IEEE/CVF conference on computer vision and pattern recognition*, pages 8922–8931.
- Tang, L., Jia, M., Wang, Q., Phoo, C. P., and Hariharan, B. (2024). Emergent correspondence from image diffusion. Advances in Neural Information Processing Systems, 36.

- Toga, A. W. and Thompson, P. M. (2001). The role of image registration in brain mapping. *Image and vision computing*, 19(1-2):3–24.
- Wang, G., Wang, Z., Chen, Y., and Zhao, W. (2015). Robust point matching method for multimodal retinal image registration. *Biomedical Signal Processing and Control*, 19:68–76.
- Wang, J. et al. (2019). Gaussian field estimator with manifold regularization for retinal image registration. *Signal Processing*, 157:225–235.
- Wang, S., You, H., and Fu, K. (2011). Bfsift: A novel method to find feature matches for sar image registration. *IEEE Geoscience and Remote Sensing Letters*, 9(4):649–653.
- Wang, Y. et al. (2020). A segmentation based robust deep learning framework for multimodal retinal image registration. In ICASSP 2020-2020 IEEE International Conference on Acoustics, Speech and Signal Processing (ICASSP), pages 1369–1373. IEEE.
- Yang, X. and Wang, X. (2023). Diffusion model as representation learner. In *Proceedings of the IEEE/CVF International Conference on Computer Vision*, pages 18938–18949.
- Zhao, D., Song, Z., Ji, Z., Zhao, G., Ge, W., and Yu, Y. (2021). Multi-scale matching networks for semantic correspondence. In *Proceedings of the IEEE/CVF International Conference on Computer Vision*, pages 3354–3364.
- Zhu, Y.-M. (2007). Mutual information-based registration of temporal and stereo retinal images using constrained optimization. *Computer methods* and programs in biomedicine, 86(3):210–215.
- Zou, B., He, Z., Zhao, R., Zhu, C., Liao, W., and Li, S. (2020). Nonrigid retinal image registration using an unsupervised structure-driven regression network. *Neurocomputing*, 404:14–25.